Hydrothermal Growth of MnO₂ at 95 ºC as an Anode Material

D. Vernardou[1,*], *A. Kazas*[2], *M. Apostolopoulou*[1], *N. Katsarakis*[1,3,4] *and E. Koudoumas*[1,3]

[1]Center of Materials Technology and Photonics, School of Applied Technology, Technological Educational Institute of Crete, 710 04 Heraklion, Crete, Greece.

[2]Mechanical Engineering Department, School of Applied Technology, Technological Educational Institute of Crete, 710 04 Heraklion, Crete, Greece.

[3]Electrical Engineering Department, School of Applied Technology, Technological Educational Institute of Crete, 710 04 Heraklion, Crete, Greece.

[4]Institute of Electronic Structure and Laser, Foundation for Research & Technology-Hellas, P.O. Box 1527, Vassilika Vouton, 711 10 Heraklion, Crete, Greece.

Abstract: The hydrothermal growth of manganese dioxide was carried out on indium tin dioxide coated glass substrates using potassium permanganate at 95 ºC for 24 h and adjusting the pH solution to 3 and 4 through nitric acid. The best capacitive response was observed from the hexagonal ε-manganese dioxide at pH 4 having a specific charge of 129 ± 1 A g^{-1} and specific discharge capacity of 943 mAh g^{-1} with capacitance retention of 98 % after 500 scans at 4 A g^{-1} presenting high rate performance and good stability. The importance of achieving crystalline electrodes with high specific surface area towards the improvement of their capacitive performance for power devices is highlighted.

Keywords: Hydrothermal growth; manganese dioxide; pH; electrochemical characteristics.

1 Introduction

Electrochemical capacitors, ultra-capacitors and electrical double layer capacitors (EDLCs) have appealed substantial attention as energy storage devices due to their higher power densities than lithium-ion batteries (LIBs), larger energy densities and longer cycle life than conventional capacitors [1-3]. Their large specific capacitance is a result of one or a combination of double-layer capacitance and charge-transfer-reaction pseudocapacitance charge-storage mechanisms [4, 5]. Double-layer capacitance arises from the separation of charge at the interface between a solid electrode and an electrolyte, while pseudocapacitance arises from fast, reversible faradaic reactions occurring at or near a solid electrolyte [1, 3-5].

The required characteristics for supercapacitor electrodes are large surface area, high conductivity and electrochemical stability. In this respect, efforts have been made by designing and optimizing various electroactive materials with desirable morphology, which are the basis for the further enhancement of electrochemical properties [6]. Potential used electrode materials are carbonaceous materials, which have high specific surface area and specific capacitances in aqueous

and non-aqueous electrolytes [7-9]. However, they have been found to suffer from high internal resistance and slow deterioration by oxidation [10]. On the other hand, multivalent metal oxides exhibit Faradaic pseudocapacitance that usually exceeds carbon-based materials [6]. Among them, manganese dioxide (MnO₂) is regarded as one promising candidate on account of its superior electrochemical performance, low cost and environmental compatibility [11-15]. The pseudocapacitance of MnO₂ is primarily produced by the fast transition Mn^{4+}/Mn^{3+} [16]. Taking into consideration the poor electrical conductivity of MnO₂, only a very thin layer of bulk MnO₂ is involved in charge storage [17]. Thus, attempts are focused to grow ultrathin MnO₂ electrode nanomaterials with enhanced charge and ion diffusion [18, 19]. In this regard, one approach is to synthesize MnO₂ nanostructured films on conducting substrates providing specific capacitance values of 595.2 F g^{-1} in 1 M KOH [20], 632 F g^{-1} in 0.5 M Na₂SO₄ [21] and 359 F g^{-1} in 6 M KOH [22]. Additionally, MnO₂ nanoflakes were deposited on C/TiO₂ shell/core nanowire arrays exhibiting a specific capacitance of 639 F g^{-1} and high specific capacity retention of up to 78.7 % after 1000 cycles [23]. Similarly, many efforts have been made to increase the surface area and electrochemical activity of MnO₂ by using a synthesis of hybrid MnO₂/nanostructured carbon compound electrodes [24-28]. For instance, the carbon nanotube/MnO₂ nanocomposite ultrathin film electrodes demonstrated a high specific capacitance of 940 F g^{-1} [29].

---

*Corresponding author E-mail: dvernardou@staff.teicrete.gr

To enable electrochemical capacitors technology for large scale applications, requires the development of low-cost energy storage systems. There are two key aspects to meet these requirements: inexpensive high-performance materials and scalable processing for low-cost fabrication. Although, MnO_2 incorporated with carbon nanotubes presents exciting properties, significant cost reduction of carbon nanotubes is still needed to realize large-scale energy storage applications. From the perspective of the fabrication process, highly scalable approaches such as facile solution-based process will be of great importance to provide a long-term solution for making large-scale and low-cost devices.

In this work, hydrothermal synthesis of MnO_2 with controllable morphology and structure was performed at 95 ºC for 24 h. Hydrothermal growth is a simple, secure technique to grow nanostructures at low temperatures [30-32]. It does not require complicated templates or catalysts and therefore can easily be scaled up to produce nanostructures without special post synthesis treatment. The influence of pH solution on the structure, morphology, which in turn affects the electrochemical properties of MnO_2 electrodes in an alkaline electrolytic solution, will be investigated.

2 Experimental

The hydrothermal growth of MnO_2 was performed using potassium permanganate ($KMnO_4$) and 1 M, nitric acid (HNO_3) to adjust the pH to 3 and 4. In particular, an aqueous solution of 0.025 M, $KMnO_4$ was transferred in a Pyrex glass bottle with the substrate positioned on the bottom and heated at 95 ºC for 24 h in a regular laboratory oven. At the end of the growth period, the working electrodes (regarded as the substrates with the MnO_2 coating on the top) were washed with MilliQ H_2O (MilliQ refers to H_2O that has been purified and deionised by a H_2O purification system manufactured by Millipore Corporation) and dried in air at 95 ºC. Prior to deposition, all substrates (indium tin dioxide (ITO), 2 x 2 cm) were ultrasonically cleaned with propanol, acetone, MilliQ H_2O and dried with N_2.

Structural evaluation of the electrodes was carried out using x-ray diffraction (XRD) in a Siemens D5000 Diffractometer for 2-theta = 20.0 – 35.0 º, step size 0.05 º, step time 60 s/º and Raman spectroscopy in a Nicolet Almega XR micro-Raman system at 473 nm. Additionally, their morphology was studied in a Jeol JSM-7000F field-emission scanning electron microscope (FE-SEM). In this case, all samples were over-coated with a thin film of gold to make them more conductive.

The cyclic voltammetry and the electrochemical impedance spectroscopy (EIS) of the electrodes were accomplished in a three-electrode cell as reported previously [33-35]. The electrolyte was an aqueous solution of 1 M, LiOH for a scan rate of 10 mV s^{-1} through the potential range of -0.2 V to +0.7 V and number of scans up to 500. This range was limited by the need to have no remnant Li charge inside the MnO_2 at the end of each intercalation / deintercalation cycle i.e. the need to always have a closed loop in the voltammograms. The lithium ion intercalation / deintercalation process with respect to time was studied using chronoamperometry at -0.2 V and +0.7 V. Additionally, the chronopotentiometric curves were obtained at a constant specific current of 4 A g^{-1} and a potential range of -0.05 V to +0.25 V. Finally, the EIS curves were carried out with AC amplitude of 0.2 V and a set potential of -0.1 V over the frequency range of 10 mHz – 35 kHz. In all cases, the area of the working electrode exposed to the electrolyte was 1 cm^2.

3 Results and Discussion

Figure 1 (a) shows the XRD pattern of the hydrothermally grown MnO_2 at pH 4. A predominant peak at 26.68 º with Miller index (111) and two peaks with low intensity at 22.31 and 32.55 º with respective Miller indices (100) and (101) are observed due to the hexagonal ε-MnO_2 [36-38]. Additionally, a peak at 31.00 o with Miller index (222) is shown due to the underlying glass substrate [39, 40]. There was no evidence of MnO_2 diffraction peaks for the as-grown sample at pH 3 because of the partial dissolution of MnO_2 as soon as it was removed from the Pyrex bottle. A similar pattern was observed for pH 6 since in this case the coating has probably an amorphous or poorly crystalline structure.

In order to verify XRD results, Raman analysis was also accomplished as indicated in Figure 1 (b). Two peaks at 566 and 634 cm-1 are indicated for the as-grown MnO_2 at 95 ºC for pH 4 and attributed to the deformation mode of metal-oxygen chain of Mn-O-Mn in the MnO_2 octahedral lattice and the Mn-O stretching mode due to the presence of ε-MnO_2 [41]. Regarding the sample at pH 6, one peak at 655 cm^{-1} is presented, which is interpreted as Mn-O stretching mode due to γ-MnO_2 phase [42, 43]. No Raman bands observed for the as-grown sample at pH 3.

Although, XRD analysis gave no indication of MnO_2, Raman study revealed the presence of γ-MnO_2 indicating that the sample is mainly amorphous retaining however a short-range crystalline ordering [44].

The crystallinity of the as-grown MnO_2 was influenced by the presence of HNO_3 during the hydrothermal process. The hydrothermally obtained MnO_2 was amorphous γ-MnO_2 and it transformed into crystallized ε-MnO_2 after the presence of HNO_3. Lowering the pH to 3, the partial dissolution of MnO_2 resulted in such acidic medium giving amorphous MnO_2. The crystallization is believed to undergo a dissolution-recrystallization process; i.e., amorphous MnO_2 dissolved first and then condensed to recrystallize under the presence of HNO_3. In the dissolution-recrystallization mechanism, the added H^+ means more chance to serve as the template for an intergrowth of pyrolusite with (1 x 1) tunnels and ramsdellite with (1 x 2) tunnels [45] to get pure ε-MnO_2, which is in the same classification with γ-MnO_2, however with more structural faults (i.e. De Wolff faults) [46] and structural

defects (i.e. microtwinning) [47]. The dissolution-recrystallization process from amorphous MnO_2 is in agreement with the growth α- and β-MnO_2 by hydrothermally treating amorphous MnO_2 in the presence of cations such as K^+ and H^+ [48].
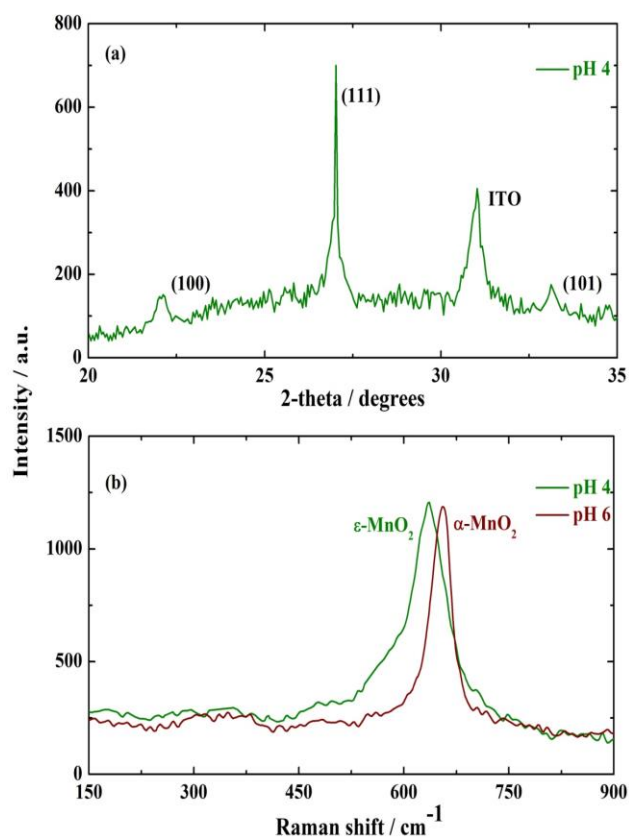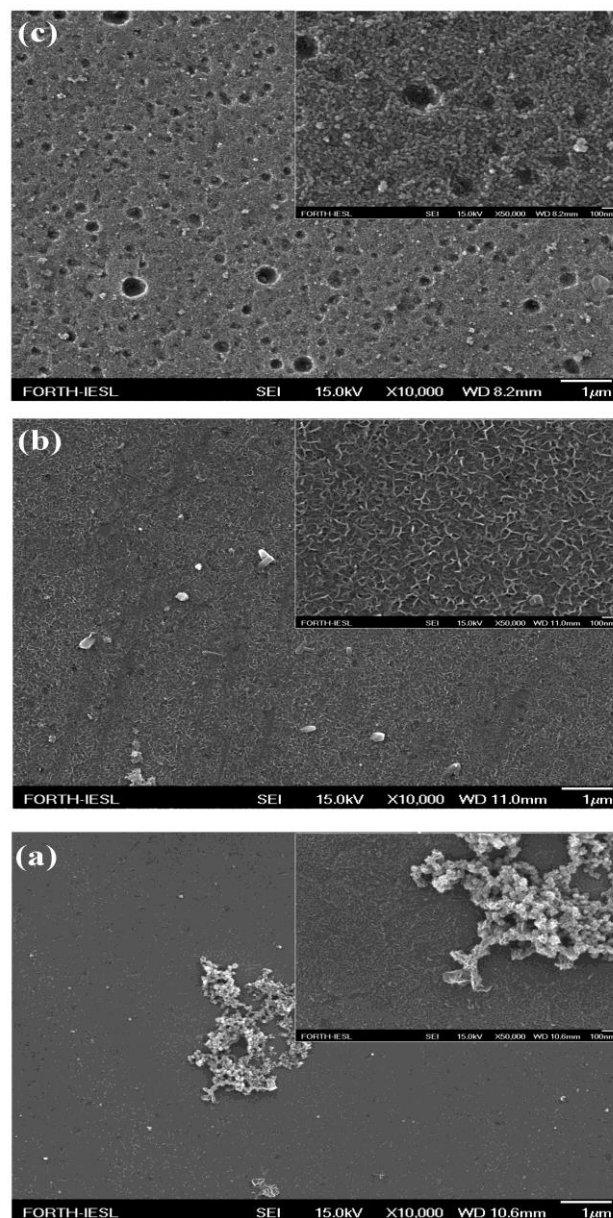

Fig. 1. (a) XRD of the hydrothermally grown MnO_2 at 95 °C for pH 4. (b) Raman spectra of the as-grown MnO_2 for pH 4 and 6.

Figures 2 (a), (b) and (c) present the FE-SEM images of the hydrothermally grown MnO_2 coatings at 95 °C for pH 3, 4 and 6 respectively. Different phases of MnO_2 samples possessed different morphologies; amorphous MnO_2 (pH 3) showed a relatively smooth layer of nanowalls and spherical aggregates of nanoparticles distributed in a small part of the material's surface due to the partial dissolution of the material, ε-MnO_2 (pH 4) presented nanowalls interconnected with each other forming a three-dimensional network and amorphous γ-MnO_2 (pH 6) was composed of spherical aggregates interconnected with each other forming a compact coating.

In order to examine the pH effect on the electrochemical performance of the coatings, cyclic voltammetry experiments were conducted as indicated in Figure 3. All curves are normalized to the mass of the working electrode resulting in units of A g^{-1}. The mass of the as-grown MnO_2 was measured by a 5-digit analytical grade scale and found to be 0.00001 g, which was obtained by measuring the ITO glass substrate before and after the growth. It can be

observed that the as-grown working electrode for pH 4 presents two redox peaks centered at -0.07 V and +0.47 V (vs. Ag/AgCl), which can be assigned to the reversible Li^+ intercalation / deintercalation process [49].

Fig. 2. FE-SEM images of hydrothermally grown MnO_2 at 95 °C for (a) pH 3, (b) pH 4 and (c) pH 6. Magnification of x50,000 is also indicated as inset for each of the respective samples.

Additionally, it becomes evident from Figure 3 that the specific current-potential curve of this sample is the highest presenting an enhanced electrochemical activity. On the other hand, the specific current of the others shows less distinctive peaks, which may be due to the lack of requisite ion injection sites. In particular, the as-grown coating for pH 3 indicated a specific current with four degrees of magnitude

lower than the pH 4 due to the immediate dissolution of the oxide by the electrolyte. Since, the electrochemical cell is made up of glass, these changes could be observed during the measurements. Finally, the shape of the cyclic voltammogram curve for pH 6 is different compared with the pH 4, which is ought to the existence of amorphous γ-MnO₂. One may then suggest from the above that the high amount of incorporated charge is a combination of both structure (increased crystalline quality) and morphology (high surface area of the nanowalls).
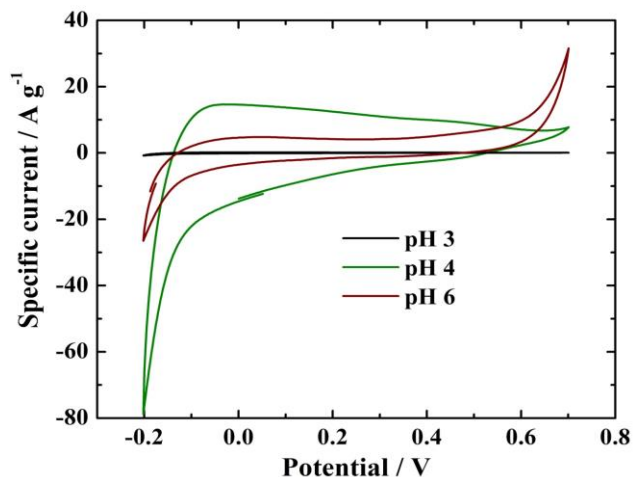

Fig. 3. Cyclic voltammograms of the first scan for the hydrothermally grown MnO₂ at 95 °C for 24 h at pH 3, 4 and 6, scan rate of 10 mV s⁻¹ and an electrode area of 1 cm².

Figure 4 (a) shows the cyclic voltammogram curves of the hydrothermally grown MnO₂ for pH 4 within a potential range from -0.2 V to +0.7 V at scan rates 2 – 200 mV s⁻¹. The peak current increases with the scan rate remaining the original shape of the curves, which suggests the fast interfacial redox reactions and rates of electronic and ionic transport [50]. Finally, the peak position shifts to lower potential as the scan rate increases, which is attributed to the polarization effect of the electrode [51]. A similar behavior is shown for the as-grown MnO₂ at pH 6 (Figure 4 (b)), but with obvious discrepancies in the shape of the curves for scan rates greater or equal with 50 mV s⁻¹ indicating the slow undesirable intercalation / deintercalation property for power devices.

To calculate the time response required and the amount of L⁺ interchanged between the MnO₂ and the electrolyte, chronoamperometric measurements were performed switching the potential between -0.2 V and +0.7 V at an interval of 200 s (per cycle) for a total period of 1600 s as indicated in Figure 5. There was a detectable decrease of interchanged charge per cycle of the order of 40 and 60 % for pH 6 and 3, respectively (not shown here for brevity) after 1000 s. The highest amount of specific charge was 129 ± 1 A g⁻¹ for ε-MnO₂ (pH 4), which was three times higher than that of amorphous γ-MnO₂ (pH 6) (see Figure 6). All charges have been estimated based on the first five cycles.
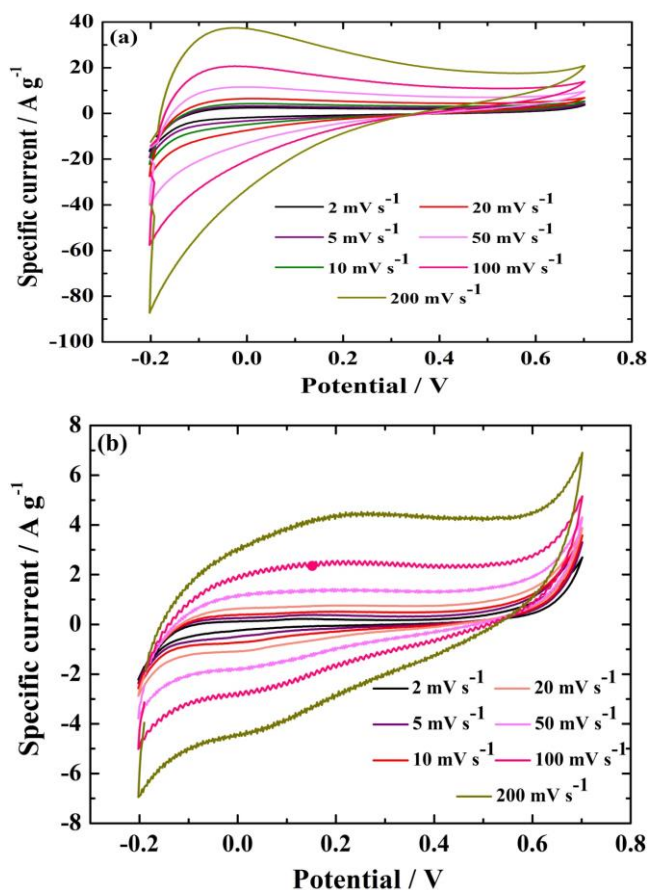

Fig. 4. Cyclic voltammogram curves of the hydrothermally grown MnO₂ for (a) pH 4 and (b) pH 6 at different scan rates.
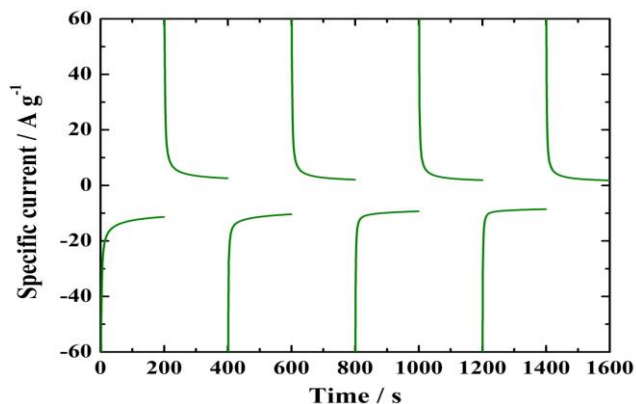
Fig. 5. The chronoamperometric response at -0.2 V and +0.7 V for an interval of 200 s of the hydrothermally grown MnO₂ at 95 °C for 24 h and pH 4.

If we define the time response (t_c) as the time needed for excess current to reduce to 10 % of its absolute maximum value [35] then Li⁺ intercalation for ε-MnO₂ (pH 4) proceeds with a t_c of 8 ± 1 s, while deintercalation is slightly slower 10 ± 1 s. Both processes in amorphous γ-MnO₂ (pH 6) have a t_c of approximately 50 ± 5 s. Cation reaction for the hydrothermally grown ε-MnO₂ is therefore much faster compared to amorphous γ-MnO₂. Surface morphology of ε-

MnO_2 incorporates more empty spaces between the nanowalls than those left by the compact coating formed from the spherical aggregates interconnected with each other, a feature that may further facilitate charge transport between the electrode and the electrolyte.
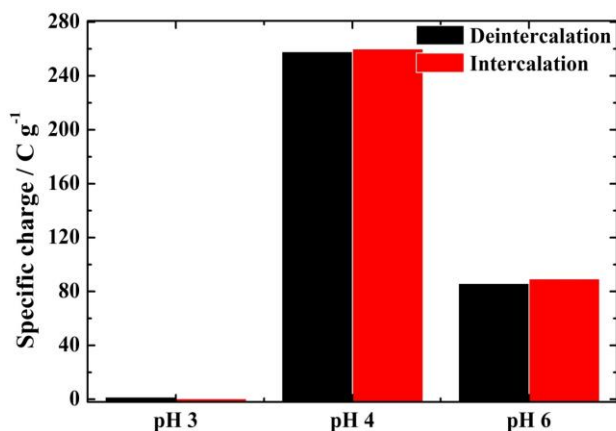

Fig. 6. Intercalated and deintercalated specific charge as a function with the pH solution.

The specific discharge capacity of the as-grown MnO_2 for pH 4 and 6 was estimated using chronopotentiometric measurements under constant specific current of 4 A g^{-1} and potential ranging -0.25 V to -0.05 V as shown in Figure 7. The discharging process of the pH 4 coating shows one obvious plateau at approximately -0.17 V and specific discharge capacity of 943 mAh g^{-1} with capacitance retention of 98 % after 500 scans (Figure 7 inset), which is promising for practical applications in lithium ion batteries and supercapacitors. On the other hand, the pH 6 lacks the staircase-like shape suggesting less-defined transition associated with Li^+. The estimated capacitance for pH 4 is higher than the hydrothermally grown α-, β-, δ- and ε-MnO_2 [45, 52], while on the same order of magnitude with the interconnected porous NiO@MnO_2 nanosheets synthesized on Ni foam [53].

Nyquist plot for the as-grown MnO_2 at pH 4 are indicated in Figures 8 (a) and (b) (maximized frequency region). The symbols represent the experimental data, while the solid lines, the results fitted by Z-view software. The as-grown coating exhibits an arc in the high frequency region and a sloped line in the low frequency region, which can be fitted by an equivalent circuit as shown in Figure 8 (a) inset. The equivalent circuit consists of bulk solution resistance R_e, the charge transfer resistance R_{ct} and the Warburg resistance (W) related to the diffusion of ions and the constant phase element (CPE) to account for the double layer capacitance [54, 55]. The diameter of the semicircle is 1 Ω, which is a quite low value and beneficial for the charge transfer across the ε-MnO_2 / electrolyte interface enhancing its capacitive performance.
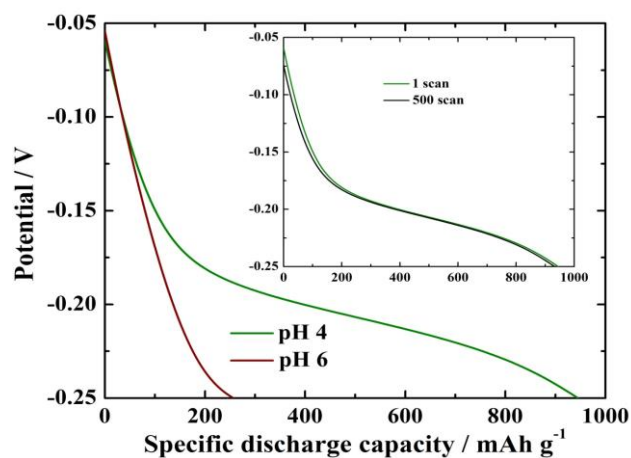
Fig. 7. The chronopotentiometric curves for MnO_2 at pH 4 (500th scan is included as inset) and pH 6 under constant specific current of 4 A g^{-1} and potential ranging from -0.25 V to -0.05 V.
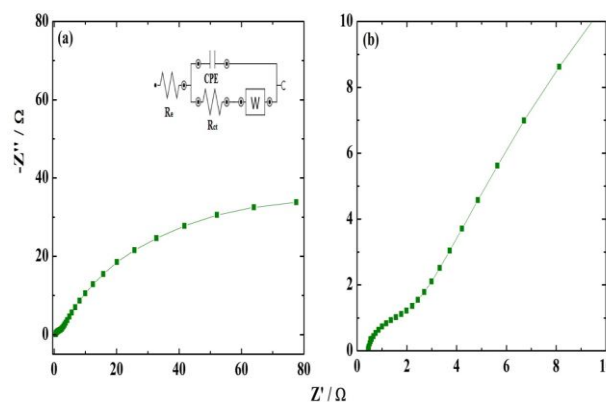
Fig. 8. (a) Nyquist plot of the measured (plot) and fitted (line) impedance spectra of the MnO_2 sample grown at 95 ºC for pH 4 and (b) the maximized high frequency region of the plot. Equivalent circuit is indicated.

4 Conclusions

Hexagonal ε-MnO_2 nanowalls were hydrothermally grown at 95 ºC for 24 h and pH 4. The particular pH is responsible for the enhanced capacitive performance of the sample due to the increased crystallinity and high surface area of the structures, which improves the ease of Li^+ intercalation / deintercalation accelerating the charge transport between the electrode and the electrolyte. Specific charge was 129 ± 1 A g^{-1} with respectable intercalation and deintercalation response times of 8 ± 1 s and 10 ± 1 s. additionally, the hydrothermally ε-MnO_2 electrode has unique characteristics including the high specific discharge capacity of 943 mAh g^{-1} with capacitance retention of 98 % after 500 scans indicating a good stability. Having demonstrated that the hydrothermal growth is a viable method for deposition of high quality materials, future work will be the transfer in flexible electrodes.

References

[1] L. L. Zhang, R. Zhou, X. Zhao, J. Mater. Chem., 2010, **20**, 5983-5992.

[2] R. Kötz, M. Carlen, Electrochim. Acta, 2000, **45**, 2483-2498.

[3] Z. K. Ghouri, N. A. Barakat, A. -M. Alam, M. Park, T. H. Han, H. Y. Kim, Int. J. Electrochem. Sci., 2015, **10**, 2064-2071.

[4] Z. Gao, J. Wang, Z. Li, W. Yang, B. Wang, M. Hou, Y. He, Q. Liu, T. Mann, P. Yang, M. Zhang, L. Liu, Chem. Mater., 2011, **23**, 3509-3516.

[5] Q. Xiao, X. Zhou, Electrochim. Acta, 2003, **48**, 575-580.

[6] T. Zhu, Z. He, G. Zhang, Y. Lu, C. Lin, Y. Chen, H. Guo, J. Alloy. Compd., 2015, **644**, 186-192.

[7] X. H. Cao, Y. M. Shi, W. H. Shi, G. Lu, X. Huang, Q. Y. Yan, Q. C. Zhang, H. Zhang, Small, 2011, **7**, 3163-3168.

[8] A. Izadi-Najafabadi, T. Yamada, D. N. Futaba, M. Yudasaka, H. Takagi, H. Hatori, S. Iijima, K. Hata, ACS Nano, 2011, **5** 811-819.

[9] K. S. Xia, Q. M. Gao, J. H. Jiang, J. Hu, Carbon, 2008, **46**, 1718-1726.

[10] S. -C. Pang, M. A. Anderson, T. W. Chapman, J. Electrochem. Soc., 2000, **147**, 444-450.

[11] D. L. Yan, H. Zhang, S. C. Li, G. S. Zhu, Z. M. Wang, H. R. Xu, A. B. Yu, J. Alloy. Compd., 2014, **607**, 245-250.

[12] Z. X. Song, W. Liu, M. Zhao, Y. J. Zhang, G. C. Liu, C. Yu, J. S. Qiu, J. Alloy. Compd., 2013, **560**, 151-155.

[13] S. M. Sun, P. Y. Wang, Q. Wu, S. Wang, S. M. Fang, Mater. Lett., 2014, **137**, 206-209.

[14] H. Jiang, C. Li, T. Sun, J. Ma, Chem. Commun., 2012, **48,** 2606-2608.

[15] P. K. Nayak, N. Munichandraiah, Micropor. Mesopor. Mater., 2011, **143**, 206-214.

[16] S. Sun, P. Wang, Q. Wu, S. Wang, S. Fang, Mater. Lett., 2014, **137**, 206-209.

[17] M. Winter, R. J. Brodd, Chem. Rev., 2004, **104**, 4245-4269.

[18] R. S. Kalubarme, H. S. Jadhav, C. J. Park, Electrochim. Acta, 2013, **87**, 457-467.

[19] A. Yu, I. Roes, A. Davies, Z. Chen, Appl. Phys. Lett., 2010, **96**, 253105.

[20] M. Huang, X. L. Zhao, F. Li, L. L. Zhang, Y. X. Zhang, J. Power Sources, 2015, **277**, 36-43.

[21] Z. Su, C. Yang, B. H. Xie, Z. Y. Lin, Z. X. Zhang, J. P. Liu, B. H. Li, F. Y. Kang, C. P. Wong, Energy Environ. Sci., 2014, **7**, 2652-2659.

[22] T. Zhu, S. J. Zheng, Y. G. Chen, J. Luo, H. B. Guo, Y. E. Chen, J. Mater. Sci., 2014, **49**, 6118-6126.

[23] S. Yang, K. Cheng, J. Huang, K. Ye, Y. Hu, D. Cao, X. Zhang, G. Wang, Electrochim. Acta, 2014, **120**, 416-422.

[24] Y. Liu, D. Yan, Y. Li, Z. Wu, R. Zhuo, S. Li, J. Feng, J. Wang, P. Yan, Z. Geng, Electrochim. Acta, 2014, **117**, 528-533.

[25] H. Pang, Z. Yang, J. Lv, W. Yan, T. Guo, Energy, 2014, **69**, 392-398.

[26] J. Kim, H. Ju, A. Inamdar, Y. Jo, J. Han, H. Kim, H. Im, Energy, 2014, **70**, 473-477.

[27] H. Gao, F. Xiao, C.B. Ching, H. Duan, ACS Appl. Mater. Interfaces, 2012, **4**, 2801-2810.

[28] J. Zhang, J. Zang, J. Huang, Y. Wang, G. Xin, Mater. Lett., 2014, **126**, 24-27.

[29] S. W. Lee, J. Kim, S. Chen, P. T. Hammond, Y. Shao-Horn, ACS Nano, 2010, **4,** 3889-3896.

[30] D. Vernardou, E. Spanakis, G. Kenanakis, E. Koudoumas, N. Katsarakis, Mater. Chem. Phys., 2010, **124**, 319-322.

[31] D. Vernardou, E. Stratakis, G. Kenanakis, H. M. Yates, S. Couris, M.E. Pemble, E. Koudoumas, N. Katsarakis, J. Photoch. Photobio. A, 2009, **202**, 81-85.

[32] G. Kenanakis, E. Stratakis, K. Vlachou, D. Vernardou, E. Koudoumas, N. Katsarakis, Appl. Surf. Sci., 2008, **254**, 5695-5699.

[33] D. Vernardou, D. Louloudakis, N. Katsarakis, E. Koudoumas, I. I. Kazadojev, S. O'. Brien, M. E. Pemble, I. M. Povey, Sol. Energ. Mat. Sol. C., 2015, **143**, 601-605.

[34] D. Vernardou, K. Psifis, D. Louloudakis, G. Papadimitropoulos, D. Davazoglou, N. Katsarakis, E. Koudoumas, J. Electrochem. Soc., 2015, **162**, H579-H582.

[35] D. Vernardou, P. Paterakis, H. Drosos, E. Spanakis, I. M. Povey, M. E. Pemble, E. Koudoumas, N. Katsarakis, Sol. Energ. Mat. Sol. C., 2011, **95**, 2842-2847.

[36] C. -H. Kim, Z. Akase, L. Zhang, A. H. Heuer, A. E. Newman, P. J. Hughes, J. Solid State Chem., 2006, **179**, 753-774.

[37] R. B. Valim, M. C. Santos, M. R. V. Lanza, S. A. S. Machado, F. H. B. Lima, M. L. Calegaro, Electrochim. Acta, 2012, **85**, 423-431.

[38] Y. Liu, H. Wang, Y. Zhu, X. Wang, X. Liu, H. Li, Y. Qian, Solid State Commun., 2009, **149**, 1514-1518.

[39] N. C. Silva Vieira, E. G. Ramos Fernandes, A. A. Alencar de Queiroz, F. E. Gontijo Guimarães, V. Zucolotto, Mater. Res., 2013, **16**, 1156-1160.

[40] D. Choi, S. -J. Hong, Y. Son, Mater., 2014, **7,** 7662-7669.

[41] P. Ragupathy, H. Vasan, N. Munichandraiah, J. Electrochem. Soc., 2008, **155,** A34-A40.

[42] Y. Xie, Y. Yu, X. Gong, Y. Guo, Y. Guo, Y. Wang, G. Lu, Cryst. Eng. Comm., 2015, **17**, 3005-3014.

[43] C. Julien, M. Massot, S. Rangan, M. Lemal, D. Guyomard, J. Raman Spectrosc., 2002, **33**, 223-228.

[44] M. Ocãna, J. V. Garcia, J. Am. Chem. Soc., 1992, **75**, 2010-2012.

[45] D. Li, G. Du, J. Wang, Z. Guo, Z. Chen, H. Liu, J. Chinese Chem. Soc., 2012, **59**, 1211-1215.

[46] P. De Wolff, J. Visser, R. Giovanoli, R. Brutsch, Chimia, 1978, **32**, 257-259.

[47] Y. S. Ding, X. F. Shen, S. Gomez, H. Luo, M. Aindow, S. L. Suib, Adv. Funct. Mater., 2006, **16**, 549-555.

[48] X. Huang, D. Lv, H. Yue, A. Attia, Y. Yang, Nanotechnology, 2008, **19**, 225606-7.

[49] A. Yuan, Q. Zhang, Electrochem. Commun., 2006, **8,** 1173-1178.

[50] H. Wang, H. Yi, X. Chen, X. Wang, J. Mater. Chem. A, 2014, **2**, 1165-1173.

[51] X. -J. Ma, W. -B. Zhang, L. -B. Kong, Y. -C. Luo, L. Kang, RSC Adv., 2015, **5**, 97239-97247.

[52] X. Duan, J. Yang, H. Gao, J. Ma, L. Jiao, W. Zheng, Cryst. Eng. Commun., 2012, **14**, 4196-4204.

[53] X. Shang, X. Li, H. Yue, S. Xue, Z. Liu, X. Hou, D. He, Mater. Lett., 2015, **57**, 7-10.

[54] A. Di Fabio, A. Giorgi, M. Mastragostino, F. Soavi, J. Electrochem. Soc., 2001, **148**, A845-A850.

[55] J. Gamby, P.L. Taberna, P. Simon, J.F. Fauvarque, M. Chesneau, J. Power Sources, 2001, **101**, 109-116.